JOURNAL OF COMPUTATIONAL PHYSICS 35, 291–318 (1980)

A Numerical Model for Laser Targets

J. P. CHRISTIANSEN

Euratom/UKAEA Fusion Association, Culham Laboratory, Abingdon, Oxon. OX14 3DB, United Kingdom

AND

N. K. WINSOR

Naval Research Laboratory, Washington D.C.

Received December 20, 1978; revised July 18, 1979

A two-dimensional, three-temperature MHD model for numerical calculations of the dynamics of laser targets is described. Time-dependent atomic physics, transport of continuum radiation by a diffusion approximation, and self-generated magnetic fields are included in the description. Various numerical methods for solving the finite-difference equations are outlined and compared. Results from these calculations show that magnetic source terms and thermal conductivity terms must be treated with great care if proper energy balance is to be maintained between the magnetic field and the electrons.

1. INTRODUCTION

In the last few years there has been a considerable effort in the numerical modeling of laser-produced plasmas. Such numerical calculations of laser-produced plasmas are essential in feasibility studies of laser fusion [1] and X-ray sources [2]. Several computer codes have been described by other authors: one-dimensional compression and transport codes [3–5], two-dimensional transport [6, 7], and compression codes [8, 9]. The physical models used by these codes emphasize some aspects of the target physics, while many other aspects may be omitted depending on the specific application of the code. Consequently the numerical methods employed by each of these laser target codes differ substantially so that a straightforward comparison between these codes is difficult.

In this paper we describe the details of a laser-target model and present results from calculations with this model. In the calculations various numerical methods have been tried. We discuss our experience with these methods. The model described in this paper is used in a code named CASTOR [10]. It is generally similar to the models used in [6, 7, 11]. Certain parts of the physics are simplified or omitted as outlined in the following. The equations used are presented in sections 2–4. Sections 5–10 and the Appendix describe various numerical methods and their performance. Results from

0021-9991/80/060291-28$02.00/0

calculations with the code are shown in Section 11 and comparisons are made between the numerical methods tried.

The purpose of the CASTOR code is to study the basic plasma properties of an expanding laser-produced plasma with an emphasis on atomic physics, radiation emission, transport of thermal and radiation energy, generation of magnetic fields, and their effects upon the plasma. In this respect the code resembles the codes of [6, 7]. Two-dimensional cylinder geometry (r, z) is assumed as illustrated in Fig. 1. The laser target is assumed to be a single element of moderate atomic Z. The present studies are for carbon ($Z = 6$). The state of the target can be obtained from either perfect gas laws, a coronal equilibrium model [12], or a time-dependent ionization recombination model [13]. The laser pulse is characterized by the wavelength λ_L, the available pulse energy E_L, and the power illumination profile $P_L(r, t)$ where t denotes time. A straight-line approximation is used such that the laser beam travels parallel to the z-axis. The plasma produced by the laser is described via the set of MHD equations derived by Braginskii [14] in the variables ρ (mass density), $\rho\mathbf{u}$ (momentum, ϵ (energy density), $\mathbf{B}$ (magnetic field), T_e (electron temperature), and T_i (ion temperature). The continuum radiation field is described via a radiation temperature T_R, while the emitted line radiation is purely calculated from the equation of state as a loss mechanism.

The MHD equations are solved on an Eulerian grid using the flux-corrected transport method of Boris and Book [16]. Although the grid can move as a result of a dynamic rezoning technique similar to that of [17], the grid lines remain orthogonal. Large-scale hydrodynamics, e.g., compression, will probably not be treated as well by our approach as by a full Lagrangian description like that of [8]. The grid size is $0 < r < R_0$ and $z_1 < z < z_2$.

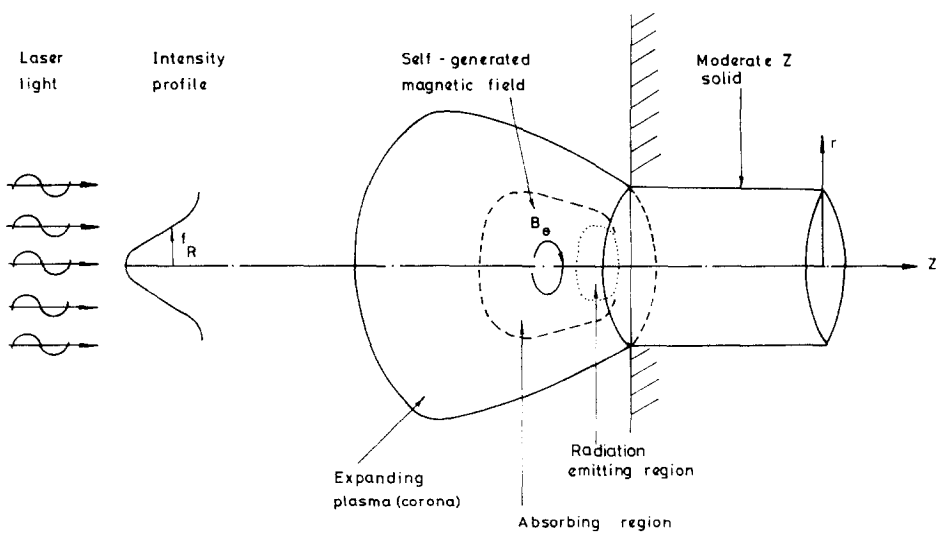

FIG. 1. Schematic laser target model showing (r, z) cylinder geometry.

The fundamental philosophy behind our numerical treatment of the equations involved is the division of the physical effects into two categories. (I) entropy generating processes and (II) adiabatic processes. This division is reflected in the calculation cycle which is split into two distinct stages. The transport equations (20)–(22) and (27) are written so that the left-hand sides represent terms of stage II, while terms on the right-hand sides are treated during stage I. All quantities are expressed in SI units, though temperatures may be quoted in eV.

2. Equations of State

The target plasma consists of partly ionized ions of density n_i, mass number M, and free electrons of density n_e. The fractional population density of j times ionized atoms is f_j, and averages are denoted as follows:

$$\langle \psi \rangle = \sum_{j=0}^{Z} f_j \psi_j \tag{1}$$

indicating a weighted average of ψ over all ionization stages. The vector $\mathbf{f} = (f_0, f, ..., f_Z)$ obeys the equation [13]

$$\frac{\partial \mathbf{f}}{\partial t} + (\mathbf{u} \cdot \nabla) f = \underline{\mathbf{A}} \cdot \mathbf{f}, \tag{2}$$

where the matrix $\underline{\mathbf{A}}$ contains the ionization and recombination rates and $\mathbf{u}$ is the velocity defined in Section 4. Electrical neutrality of the plasma,

$$n_e = \langle z \rangle n_i, \tag{3}$$

is assumed and all ion states have the same temperature T_i. The internal energy is

$$\epsilon = \tfrac{3}{2} n_i k (T_i + \langle z \rangle T_e) + \langle E_z \rangle n_i, \tag{4}$$

where $\langle E_z \rangle$ is the energy required to form a mean ionization level $\langle z \rangle$. From (4) the specific heats are obtained,

$$C_{vi} = \frac{3}{2} n_i k, \qquad C_{ve} = \frac{3}{2} n_e k + n_i \frac{\partial \langle E_z \rangle}{\partial T_e}, \tag{5}$$

and the plasma pressure,

$$p = n_i k T_i + n_e k T_e = p_i + p_e. \tag{6}$$

3. Emission of Radiation

The treatment of radiation arising from bound–bound (bb), free–bound (fb), and free–free (ff) transitions is simplified as follows. The radiation rates are written as

$$P_{\mathrm{bb}} = C_{\mathrm{bb}} T_e^{-1/2} n_i^2 \langle z \rangle \langle e^{-\delta_z} \rangle, \tag{7}$$

$$P_{\mathrm{fb}} = C_0 T_e^{1/2} n_i^2 \langle z \rangle \langle z^2 \delta_z \rangle, \tag{8}$$

$$P_{\mathrm{ff}} = \tfrac{1}{2} C_0 T_e^{1/2} n_i^2 \langle z \rangle \langle z^2 \rangle, \tag{9}$$

where $\delta_z = (E_g - E_z)/kTe$ is the normalized energy gap between the ground state and state z_0 . The expressions for the numerical constants C_{bb} and C_0 can be found in [12, 13].

A fraction $1 - (n_e/n_{eL})^2$ of the line radiation is assumed to escape the plasma for $n_e < n_{eL}$, where n_{eL} is a density chosen below the solid density (typically n_{eL} is 10–20 % of the solid density). For $n_e > n_{eL}$ the line radiation is assumed to be reabsorbed.

Transport of continuum radiation energy occurs via a diffusion approximation similar to that of [5]. In terms of the radiation energy intensity $\epsilon_R = aT_R^4$ we solve [18]

$$\frac{\partial \epsilon_R}{\partial t} = -\nabla \cdot \mathbf{F}_R + S_R , \tag{10}$$

where the radiative flux F_R is of the form

$$\mathbf{F}_R = -\kappa_R \nabla \epsilon_R \tag{11}$$

and S_R the transfer rate of energy between the electrons and the radiation field. The diffusivity used is (c denotes the speed of light)

$$\kappa_R = \frac{4c}{3\rho K_R} , \tag{12}$$

where ρ is the mass density and K_R is the opacity (e.g., Kramers opacity [19]). S_R is the difference between emission by the electrons of radiation with a Planckian intensity

$$B_\nu(T_e) = \frac{2h\nu}{c^2} (e^{h\nu/kT_e} - 1)^{-1} \tag{13}$$

and reabsorption of the local radiation field (inverse Bremsstrahlung) with a Planck distribution $B_\nu (T_R)$. S_R is obtained after an integration over all frequencies and for computational purposes [5] expressed in the form

$$S_R = \frac{1}{T_e} (P_{\mathrm{ff}} + P_{\mathrm{fb}})(T_e - T_R)\, G(T_R/T_e). \tag{14}$$

where $G(T_R/T_e)$ is given in [5].

In optically thin regions, where $\lambda_R = 1/\rho K_R \gg R_0$, S_R does not enter (10) but $P_{ff} + P_{fb}$ is included as radiation loss in the electron energy equation. The total emission from the plasma comprises the contribution from optically thin regions

$$\Psi(\lambda_R \gg R_0) = 2\pi \int_{z_1}^{z_2} \int_0^{R_0} (P_{ff} + P_{fb})\, r\, dr\, dz, \tag{15}$$

and the radiation leaving the plasma surface, where T_R is fixed at Troom

$$\Psi = \int_s (-\kappa_R \nabla \epsilon_R)\, da. \tag{16}$$

The spectral distribution of the emitted XUV radiation Ψ is given by (13).

4. MHD Equations

The MHD equations solved are those derived by Braginskii [14]. Ions and electrons are treated as one fluid of mass density

$$\rho = n_i M m_p + n_e m_e, \tag{17}$$

m_p and m_e being the proton and electron rest masses, and M the atomic mass of the ions. The fluid moves with a velocity

$$\mathbf{u} = \frac{M m_p \mathbf{u}_i + m_e \mathbf{u}_e}{M m_p + m_e} \simeq \mathbf{u}_i. \tag{18}$$

The electrical current density is

$$\mathbf{J} = \frac{1}{\mu_0} \nabla \times \mathbf{B} \equiv -e n_e \mathbf{u}_J \tag{19}$$

which defines the "current" velocity $\mathbf{u}_J$. The equations of mass and momentum conservation are

$$\frac{\partial \rho}{\partial t} + \nabla \cdot \rho \mathbf{u} = 0, \tag{20}$$

$$\frac{\partial \rho \mathbf{u}}{\partial t} + \nabla \cdot \rho \mathbf{u}\mathbf{u} = -\nabla p + \mathbf{J} \times \mathbf{B} + \nabla_z \frac{1}{c} F_L, \tag{21}$$

where the laser flux F_L is in the z-direction ($\nabla_z = \partial/\partial z$). The equation for the total internal energy

$$\frac{\partial \epsilon}{\partial t} + \nabla \cdot \epsilon \mathbf{u} + p \nabla \cdot \mathbf{u} = -\nabla \cdot \mathbf{F} - \nabla \cdot \mathbf{F}_L - S_R - P_{bb} + \mathbf{E} \cdot \mathbf{J} \tag{22}$$

is supplemented by an ion energy equation ($\epsilon_i = C_{vi}T_i$)

$$\frac{\partial \epsilon_i}{\partial t} + \nabla \cdot \epsilon_i \mathbf{u} + p_i \nabla \cdot \mathbf{u} = -\nabla \cdot \mathbf{F}_i + K. \tag{23}$$

In (22) $\mathbf{F} = \mathbf{F}_e + \mathbf{F}_i$ is the total thermal flux including the thermo electric flux and

$$\mathbf{F}_e = -\underline{\varkappa}_e \cdot \nabla T_e - \frac{kT_e}{e} \underline{\beta} \cdot \mathbf{J}, \tag{24}$$

$$\mathbf{F}_i = -\underline{\varkappa}_i \cdot \nabla T_i, \tag{25}$$

the transport tensors being given in [14]; P_{bb} is the line radiation loss and S_R is already given. The energy exchange rate between ions and electrons K has the form [14, 20]

$$K = \frac{3}{2} n_e k \frac{1}{\tau_{eq}} (T_e - T_i). \tag{26}$$

The transfer rate of energy $\mathbf{E} \cdot \mathbf{J}$ between the magnetic field and the electrons is calculated from

$$\frac{\partial \mathbf{B}}{\partial t} - \nabla \times \mathbf{u} \times \mathbf{B} = -\nabla \times \mathbf{E}, \tag{27}$$

where the electric field is [14]

$$\mathbf{E} = \underline{\eta} \cdot \mathbf{J} + \mathbf{E}_s, \tag{28}$$

$$\mathbf{E}_s = -\frac{kT_e}{en_e} \nabla n_e - \frac{k}{e} \underline{\beta} \cdot \nabla T_e + \frac{1}{en_e} \mathbf{J} \times \mathbf{B}. \tag{29}$$

As shown in [2, 6, 15, 21] asymmetries in the laser-illumination profile can produce a magnetic field (see Fig. 1) via the first two terms in (29). In (r, z) cylinder geometry this field becomes $\mathbf{B} = (0, B_\theta, 0)$ so that (27) reduces to a scalar equation.

The laser light incident on the target has a flux $F_0^+ = F^+(r, z = z_1, t)$ and absorption occurs via inverse Bremsstrahlung [22] at electron densities below the critical density

$$n_c = \frac{\epsilon_0 m_e}{e^2} \left(\frac{2\pi c}{\lambda_L}\right)^2. \tag{30}$$

The classical absorption coefficient α is given in [22] and written in the form

$$\alpha = \frac{(2\pi m_e)^{1/2} e^2 c}{\epsilon_0 k^{3/2}} \frac{\langle z \rangle}{\lambda_L^2} \frac{\xi^2}{(1 - \xi)^{1/2}} \frac{\ln \Lambda_{ei}}{T_e^{3/2}}, \tag{31}$$

where $\xi = n_e/n_c$. The flux reaching the critical depth z_c at which $n_e = n_c$ is

$$F_c = F_0^+ e^- \int_{z_1}^{z_c} \alpha \, dz = F_0^+(1 - A_0). \tag{32}$$

F_c can be split into two parts: $A_c F_c$ deposited at z_c and a reflected flux $(1 - A_c) F_c$. The flux reflected by the plasma is

$$F_0^- = F_0^+ (1 - A_c)(1 - A_0)^2.$$

5. Time Splitting of Diffusion and Hydrodynamics

The principal variables ρ, $\rho\mathbf{u}$, ϵ, T_e, T_i, T_r, and B are all known at the same points on an orthogonal (r, z) mesh shown in Fig. 2. The mesh is of dimensions $N_r \times N_z$ and indices (i, j) refer to an (r, z) position. To make the notation and in particular the subscripts as compact as possible we adopt in the following a notation for referring to mesh points as is illustrated in Fig. 2. Quantities Q at point (i, j) are either referred to as Q or $Q_{0,0}$; $Q(i + \frac{1}{2}, j)$ becomes $Q_{+,0}$; $Q(i + 1, j - \frac{1}{2})$ becomes $Q_{++,-}$ and so on (see Fig. 2). The mesh spacings are

$$\Delta r = r_+ - r_-, \qquad \Delta r_+ = r_{++} - r,$$

and similarly for Δz and Δz_+.

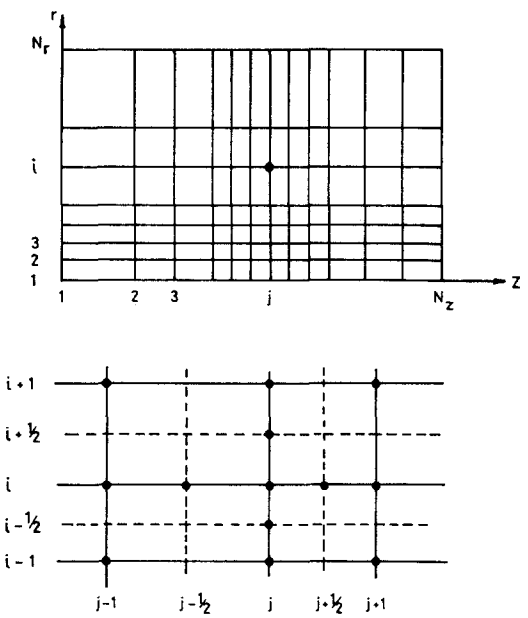

FIG. 2. The calculation mesh of $N_r \times N_z$ points is shown above. The dots indicate those neighbouring points involved in the finite difference equations for point (i, j). Displacements in the positive and negative r, z directions of half a cell width are represented by $+$ and $-$ subscripts, respectively; similarly displacements of a full cell width, by $+ +$ and $- -$, subscripts. Thus a quantity Q at point $(i, j + \frac{1}{2})$ becomes $Q_{0,+}$, at point $(i - 1, j + 1) Q_{--,++}$ and so on.

One cycle in the calculation consists of integrating Eqs. (2), (10), (20)–(23), and (27), one step Δt forward in time. The cycle is split into two parts as mentioned earlier so that the time derivatives are approximated as follows:

$$\frac{\partial}{\partial t} = \left(\frac{\Delta}{\Delta t}\right)_{\mathrm{I}} + \left(\frac{\Delta}{\Delta t}\right)_{\mathrm{II}}. \tag{33}$$

Subscript I refers to the changes caused by the terms on the RHS of the equations; stage I is the diffusion stage. Subscript II refers to the changes caused by the terms on the LHS of the transport equations; stage II is the hydrodynamic stage. Equation (33) implies an overall first order accuracy with respect to the step length $\Delta t = t^{n+1} - t^n$. Superscripts $n + 1$ and n refer to the value of a quantity at times t^{n+1} and t^n.

6. The Two Stages of Calculation

6.1. *The Hydrodynamic Calculation*

The second stage of the calculation cycle solves equations (20)–(22) and (27) in the form

$$\left(\frac{\Delta Q}{\Delta t}\right)_{\mathrm{II}} + A_r Q + A_z Q + HQ = 0, \tag{34}$$

where Q denotes ρ, ρu, ϵ, and B, respectively. The advection operators on a cylindrical mesh are (see Fig. 2)

$$(A_r Q)_{0,0} = \frac{1}{r(r_{++} - r_{--})}\left[(ru_r Q)_{++,0} - (ru_r Q)_{--,0}\right], \tag{35}$$

$$(A_z Q)_{0,0} = \frac{1}{z_{++} - z_{--}}\left[(u_z Q)_{0,++} - (u_z Q)_{0,--}\right]. \tag{36}$$

Equation (34) is solved by the FCT algorithms of Boris and Book [16] and a splitting in r and z is employed

$$\left(\frac{\Delta Q}{\Delta t}\right)_{\mathrm{II}} = \left(\frac{\Delta Q}{\Delta t}\right)_{\mathrm{II}r} + \left(\frac{\Delta Q}{\Delta t}\right)_{\mathrm{II}z}. \tag{37}$$

For each of the sweeps in the r or z directions a predictor–corrector scheme is used. Equation (34) is first integrated explicitly over a step length $\Delta t/2$, then u_r, u_z, and the source terms $H\{Q\}$, e.g. ∇p, $\mathbf{J} \times \mathbf{B}$, are evaluated. These time-centered values are then used to advance Eq. (34) a full step length Δt.

The FCT algorithms can advance Q^n (at step n) defined at a mesh (r^n, z^n) to Q^{n+1} at (r^{n+1}, z^{n+1}). The dynamic rezoning technique used in our model is that described in [17] such that the meshes r^{n+1} and z^{n+1} are determined from r^n, z^n, and ρ^n at the end of the previous cycle.

6.2. *The Diffusion Stage*

Equation (2) is solved by the TRIP algorithm described in [13] and will not be dealt with any further. The equations (10), (22), (23), and (27) for T_e, T_i, T_R, and B, respectively, can all be written in the compact form

$$C_j \frac{\partial Q_j}{\partial t} = D_j + D_{\wedge j} + G_{\perp j} + G_{\wedge j} + A_j + S_j, \tag{38}$$

where Q_j denotes either T_e, T_i, T_R, or B. In cylinder geometry these terms are for $Q_j = T_e$,

$$C_e = C_{Ve} = \frac{3}{2} n_e k + n_i \frac{\partial \langle E_z \rangle}{\partial T_e}, \tag{39a}$$

$$D_e = \frac{1}{r} \frac{\partial}{\partial r} r \kappa_{\perp e} \frac{\partial T_e}{\partial r} + \frac{\partial}{\partial z} \kappa_{\perp e} \frac{\partial T_e}{\partial z}, \tag{39b}$$

$$D_{\wedge e} = \frac{1}{r} \frac{\partial}{\partial r} r \kappa_{\wedge e} \frac{\partial T_e}{\partial z} - \frac{\partial}{\partial z} \kappa_{\wedge e} \frac{\partial T_e}{\partial r}, \tag{39c}$$

$$G_{\perp e} = \frac{k}{\mu_0 e} \left(-\frac{1}{r} \frac{\partial}{\partial r} r \beta_\perp T_e \frac{\partial B}{\partial z} + \frac{\partial}{\partial z} \beta_\perp T_e \frac{1}{r} \frac{\partial rB}{\partial r} \right), \tag{39d}$$

$$G_{\wedge e} = \frac{k}{\mu_0 e} \left(\frac{1}{r} \frac{\partial}{\partial r} r \beta_\wedge T_e \frac{1}{r} \frac{\partial rB}{\partial r} + \frac{\partial}{\partial z} \beta_\wedge T_e \frac{\partial B}{\partial z} \right) \tag{39e}$$

$$S_e = -P_{bb} + \mathbf{E} \cdot \mathbf{J} - \frac{\partial}{\partial z} F_L \tag{39f}$$

Further $A_e = -A_i - A_R$ (see below). For $Q_j = T_i$ we have

$$C_i = \tfrac{3}{2} n_i k \tag{40a}$$

$$G_{\perp i} = G_{\wedge i} = S_i \equiv 0 \tag{40d)–(40f}$$

$$A_i = \tfrac{3}{2} n_e k \omega_{ei} (T_e - T_i) \tag{40g}$$

and D_i, $D_{\wedge i}$ are obtained from (39b, c) by changing subscript e to i and changing $\kappa_{\wedge e}$ to $-\kappa_{\wedge i}$. The transport coefficients in (40 de) are unimportant at all T and B for moderate $-Z$ species. The source term is neglected because radiation, ohmic heating and inverse Bremsstrahlung all deposit energy predominantly in the electrons. For $Q_j = T_R$ we have

$$C_R = 4aT_R^3, \tag{41a}$$

$$D_{\wedge R} = G_{\perp R} = G_{\wedge R} = S_R = 0, \tag{41b)–(41e}$$

$$A_R = \tfrac{3}{2} n_e k \omega_{eR} (T_e - T_R), \tag{41f}$$

and D_R is given by (39b) changing subscript e to R. For $Q_j = B$ the expressions are and

$$C_b = 1, \tag{42a}$$

$$D_b = \frac{1}{\mu_0} \left(\frac{\partial}{\partial r} \eta_\perp \frac{1}{r} \frac{\partial rB}{\partial r} + \frac{\partial}{\partial z} \eta_\perp \frac{\partial B}{\partial z} \right), \tag{42b}$$

$$D_{\wedge b} = -\frac{1}{\mu_0}\left(\frac{\partial}{\partial r}\eta_\wedge \frac{\partial B}{\partial z} - \frac{\partial}{\partial z}\eta_\wedge \frac{1}{r}\frac{\partial rB}{\partial r}\right), \tag{42c}$$

$$G_{\perp b} = \frac{k}{e}\left(-\frac{\partial}{\partial r}\beta_\perp \frac{\partial T_e}{\partial z} + \frac{\partial}{\partial z}\beta_\perp \frac{\partial T_e}{\partial r}\right). \tag{42d}$$

$$G_{\wedge b} = \frac{k}{e}\left(\frac{\partial}{\partial r}\beta_\wedge \frac{\partial T_e}{\partial r} + \frac{\partial}{\partial z}\beta_\wedge \frac{\partial T_e}{\partial e}\right), \tag{42e}$$

$$S_b = -\frac{k}{e}\left(\frac{\partial}{\partial r}\frac{T_e}{n_e}\frac{\partial n_e}{\partial z} - \frac{\partial}{\partial z}\frac{T_e}{n_e}\frac{\partial n_e}{\partial r}\right), \tag{42f}$$

and

$$A_b = 0.$$

The terms (39)–(42) show how the quantities T_e, T_i, T_R, and B are coupled to each other via various physical mechanisms each with a characteristic time scale. In an expanding laser-produced plasma (see Fig. 1) there will be a significant variation (i.e., many orders of magnitude) of the variables Q_j as well as the coefficients $\kappa_\perp$, $\beta_\perp$, etc. For example, if the density n_e in the corona is 10^{-6} times n_e in the solid part of the target the coefficients scaling as n_e^2 will vary 12 orders of magnitude. On the calculation mesh covering both the corona and the solid this naturally implies that the main variables Q_j will be strongly coupled in some regions and completely decoupled in other regions. Such a feature should be reflected in the numerical treatment.

In advancing the main variables Q ($=Q_j$) from step n to step $n+1$ in stage I of the calculation, we write the left-hand side of (38) as (subscript j dropped)

$$\left(C\frac{\partial Q}{\partial t}\right)_{\mathrm{I}} = \sum_{l=1}^{m} C^n \frac{1}{\Delta t^{n+1/2}}(Q^\mu - Q^{\mu-1/m}), \tag{43}$$

where

$$\mu = n + \frac{l}{m},$$

showing that m separate steps may be involved in the integration of Q. All coefficients κ, β, η, ω, and C are evaluated at step n so that their superscript n may be dropped. The right-hand sides of Eqs. (38) for Q could be expressed in terms of Q^{n+1} only, except for the quadratic terms (39d and (39e) for which a choice between T_e and B being Q^{n+1} should be made. If all the terms (39)–(42) were expressed in terms of Q^{n+1}, this would correspond to a fully implicit treatment which retains all the coupling terms. Foregoing any discussions about the numerical stability of such a scheme one would intuitively feel that this numerical method would give less rise to trouble than other methods (see for example the discussions in [23, 24]). Indeed this method is used in one-dimensional Tokamak transport codes [25] which solve four to six coupled equations containing mostly diffusion terms and the article by Hogan [25] reviews the methods used in these MHD transport codes.

This approach has however not been pursued for several reasons: consider the set of equations which result from the finite differencing of the terms (39)–(42) using a

nine-point difference operator. On a mesh (see Fig. 2) of $M = N_r N_z$ points the set of equations can be written in the form

$$\underline{\mathbf{a}}\mathbf{Q} = \mathbf{b}. \tag{44}$$

$\mathbf{Q}$ and $\mathbf{b}$ are vectors of length $4M$, while $\underline{\mathbf{a}}$ is a nonsymmetric $4M \times 4M$ matrix with 31 bands. Contributions from D and A to $\underline{\mathbf{a}}$ are symmetric, while contributions from $D_\perp$, $G_\perp$, $G_\wedge$, and S can at best be made antisymmetric. To store elements of $\underline{\mathbf{a}}$ would require at least $4 \times 31M$ locations, probably twice that amount to account for working space. Because of the large variations in the coupling terms the convergence rates during the solution of (44) will be different for different parts of $\mathbf{Q}$, e.g., the T_i part of $\mathbf{Q}$ will converge much more rapidly than the T_e part. Therefore, the solution of (44) would be very time-consuming. In particular, a small local region of a few mesh points could slow down the convergence rate and thus hold up the progress of the physics elsewhere. Furthermore Eqs. (44) do not conserve energy exactly [26] as the transfer rate of energy $\mathbf{E} \cdot \mathbf{J}$ can only be evaluated after the equation for B has been solved.

Thus for reasons of storage limitations, computational speed, and accuracy (energy conservation) we solve Eqs. (38) separately for each quantity. To circumvent the difficulties associated with some of the coupling terms, we treat these by the fractional step method outlined above, such that more than one step, i.e., m separate steps (see Eq. (43)), is involved in the integration of Q. If no magnetic fields are present, the $D_\wedge$, $G_\perp$, and $G_\wedge$ terms of (38) vanish and no mixed derivatives are present. The resulting set of equations is solved by standard methods (Section 8). This completes one part of the diffusion stage. In the other part we deal with those terms which depend on the magnetic field. During the development of our laser-target model, these terms gave rise to numerical problems, as was also found by other authors [27]. The next section describes the various numerical methods which have been tried during the development of our laser target model and at the end of the section we summarize the method of solution.

7. Method of Solution

Magnetic fields are generated in laser-produced plasmas where the asymmetries are largest. This usually occurs at densities near the critical density [2, 21, 28]. The magnetic fields will grow and remain in regions of high conductivity, i.e., the hot corona, but quickly diffuse through the high-density resistive regions. The most important effect of the fields is on the thermal transfer of heat. The electron thermal flux will change most dramatically. As shown in [28] there may be parts of the plasma region where the terms $G_\perp$, $G_\wedge$, and S_b can generate thermal-magnetic waves, i.e., the coupling terms of (38) will admit not only diffusive solutions but also wave solutions. This property has undesirable effects on the numerical calculations if the terms $D_{\wedge b}$, $G_{\perp b}$, $G_{\wedge b}$, and S_b are treated explicitly. The best remedy is to maintain

an accurate energy balance between the electrons and the magnetic field, as we shall see below. Early calculations with our model would either come to a halt or produce meaningless results, e.g., negative values of T_e. Three problems arise in the treatment of these terms. These problems will first be discussed generally in this section, then in more detail in the Appendix. The difficulties fall in three areas: (i) spatial differencing; (ii) temporal differencing; and (iii) evaluation of $\mathbf{E} \cdot \mathbf{J}$.

The mixed derivatives can be treated in numerous ways (see for example the discussions in [23, 29]). There may be some temptation to reduce $D_{\wedge e}$ to the form

$$D_{\wedge e} = \frac{1}{r} \frac{\partial r \kappa_{\wedge e}}{\partial r} \frac{\partial T_e}{\partial z} - \frac{\partial \kappa_{\wedge e}}{\partial z} \frac{\partial T_e}{\partial r}, \tag{45}$$

and similarly for $D_{\wedge b}$, $G_{\perp}$, and $G_{\wedge}$. In (45) the r and z derivatives could then be differenced in a straightforward manner either explicitly or implicitly. The differencing is however not flux conservative and will generate or annihilate electron energy and or magnetic flux locally. Therefore the flux-conservative forms (39)–(42) should be used and this was found to be especially important for (42f), which can often be seen as written in the form (45), i.e., $S_b \sim \nabla n_e \times \nabla T_e$.

The simplest way of temporally differencing the terms $D_{\wedge}$, $G_{\perp}$, $G_{\wedge}$, and S_b is to employ explicit differences, i.e.,

$$D_{\wedge e} = D_{\wedge e}(T_e^n), \tag{46}$$

and similarly for the other terms. Explicit differencing will however cause severe restrictions on the step length Δt for the following reason. From (39b)–(39e) and (42b)–(42e) we notice that the cross derivatives can be cast in the symbolic form, e.g.,

$$D_{\wedge} = C \mid \mathbf{u}_{\wedge} \times \nabla Q \mid,$$

where ∇Q symbolically represents the operation ∇ or $\nabla \times$ on either T_e or B as appropriate. For the $D_{\wedge}$ terms $\mathbf{u}_{\wedge}$ becomes the gradient of $\rho_e u_e$, $\rho_i u_i$, $\omega_{1i} u_A$ in the strong field limit $\omega_{ce}\tau \gg 1$; u_e, u_i, and u_A are the electron thermal ion thermal and Alfven velocities, respectively, and ρ_e, ρ_i, ω_{ce}, and ω_{ci} are the Larmor radii and frequencies. Therefore if (46) is used, the step length Δt should be subject to a stability condition [30]

$$\Delta t < \Delta r / u_{\wedge}, \tag{47}$$

which is similar to the limit imposed by the advection stage of the calculation (Section 5) when $u_{\wedge}$ is replaced by the sound speed u_s. Since $u_{\wedge} \gg u_s$ can easily arise, (47) becomes a severe restriction; to overcome this a fractional steps method [30] was tried for (43) and (46) and we solved

$$Q^{\mu} = Q^{\mu - 1/m} + \frac{1}{m} \Delta t \frac{1}{C} \Sigma (Q^{\mu}), \tag{48}$$

in which $\sum$ denotes the sum $D_\wedge + G_\perp + G_\wedge$. The number m was determined so as to satisfy (47)

$$m \geqslant \left(\frac{u_\wedge}{u_s}\right)_{\max}. \tag{49a}$$

This restriction has proved prohibitively expensive on computing time; so did a "relaxed" condition allowing Q to vary $\alpha\%$ per step, i.e.,

$$m > \frac{\alpha\, \Delta t}{CQ^n} (\Sigma (Q^n))_{\max}. \tag{49b}$$

Although (48) was found not to become unstable, the limitation (49) would often be caused by a small localized low-density region which would hold up the progress of the solution elsewhere.

We have tried various combinations of implicit and explicit time differencing of the terms $D_\wedge$, $G_\parallel$, and $G_\wedge$ but we have found it necessary to treat these terms implicitly as well as the electric field E_s (Eq. (29)) in the term $\mathbf{E} \cdot \mathbf{J}$ of (39f). It is the implicit treatment of $\mathbf{E}_s(T_e) \cdot \mathbf{J}$ which was referred to as "a proper energy balance between the electrons and the magnetic field" earlier in this section (see [26]). Although this treatment complicates the finite differencing as well as the coding, it substantially improves the accuracy and progress of the calculation. Before we discuss some remaining problems we can summarize the present method of solution as follows:

$$\frac{2}{\Delta t} C_{ve}(T_e{}^\mu - T_e^{\mu-1/m}) = \Sigma_e\,(T_e{}^\mu) + \mathbf{E}_s(T_e{}^\mu) \cdot \mathbf{J}^{\mu-1/m}, \tag{50a}$$

$$\frac{2}{\Delta t} (B^\mu - B^{\mu-1/m}) = \Sigma_b\,(T_e{}^\mu) + S_b(T_e{}^\mu), \tag{50b}$$

and

$$\frac{2}{\Delta t} C_{vi}(T_i{}^\mu - T_i^{\mu-1/m}) = D_{\wedge i}(T_i{}^\mu). \tag{50c}$$

As before Σ denotes the sum $D_\wedge + G_\perp + G_\wedge$ and superscript μ indicates that two stages are present: the solutions to (50) are obtained by the ADI method using the differencing described by Marx and Killeen [23] and Lindemuth and Killeen [29].[1] During the r — sweep $\mu = n + 1/m$ (m defined below) the correct transfer rate $\mathbf{E}_s \cdot \mathbf{J}$ after the integration of (50b) is [26]

$$\mathbf{E}_s(T^\mu) \cdot \tfrac{1}{2}(\mathbf{J}^\mu + \mathbf{J}^{\mu-1/m}), \tag{51a}$$

which is not the rate of (50a). The difference,

$$\mathbf{E}_s(T^\mu) \cdot \tfrac{1}{2}(\mathbf{J}^\mu - \mathbf{J}^{\mu-1/m}), \tag{51b}$$

[1] In fact our approach resembles that of [29] since all variables which can be treated implicitly are so treated.

is evaluated and added to the RHS of (50a) during the z-sweep for which $\mu = n + 2/m$. After the z-sweep a new difference (51b) is evaluated and included in S_e for part 2.

In part 2 of the diffusion stage we solve four equations of the type (38), i.e.,

$$(1/\Delta t)\, C_v (Q^{\mu} - Q^{\mu - 1/m}) = D_{\perp}(Q^{\mu}) + A + S \qquad (52)$$

where S_j for the electrons is given by (39f) without the $\mathbf{E}_s \cdot \mathbf{J}$ term. Equation (52) can be solved either by a splitting method [30] or by the ICCG method described by Kershaw [31] together with its application to the Livermore laser code LASNEX [8]. If a splitting method is used $\mu = n + 3/m$ and $n + 4/m$ during the r- and z-sweeps of (52) and $m = 4$. If the ICCG method is used, $m = 3$ and $\mu = n + 3/m$ in (52). Equation (52) is solved first for B, then for T_e, T_i, and T_r such that the correct transfer rate (51a) ($\mathbf{E}_s$ replaced by $\eta \cdot \mathbf{J}^{\mu}$) can be evaluated after the diffusion of B.

The division of (38) into the two parts (50) and (52) may seem complicated. However, it ensures that the electric field source is solved for implicitly while at the same time energy is conserved exactly [26]. For regions where the RHS terms of (50) dominate those of (52) the solution is obtained almost fully implicitly, i.e., ΔQ of (50) is much larger than ΔQ of (52); it was precisely these regions which gave rise to problems when other methods were used.

8. Physical and Numerical Waves

To see why an implicit treatment of $\mathbf{E} \cdot \mathbf{J}$ in (39f) is used it is illuminating to consider a thermal magnetic wave (see for example the treatment by Pert [28]). Thermal magnetic waves may arise from the $D_{\wedge}$, $G_{\perp}$, $G_{\wedge}$, and S_b terms of (38) and for simplicity we look only at the electron pressure contribution to $\mathbf{E}$ (Eq. (29)) assuming n to vary in z. This reduces Eq. (38) to

$$C_v \frac{\partial T_e}{\partial t} = E_z J_z , \qquad (53)$$

$$\frac{\partial B}{\partial t} = \frac{\partial}{\partial r} E_z , \qquad (54)$$

where

$$E_z = -\frac{kT_e}{e} \frac{\partial}{\partial z} \ln n_e , \qquad (55)$$

The frequency response from the plasma to perturbations

$$T_e = T_0 + T_1 J_0(\alpha r)\, e^{i\omega t}, \qquad B = B_0 + B_1 J_1(\alpha r)\, e^{i\omega t},$$

where J_0 and J_1 are the Bessel functions, is given by

$$\omega^2 = \frac{2}{3n_e} \frac{kT_e}{e} \zeta^2 \frac{1}{e\mu_0} \alpha^2. \qquad (56)$$

We have set $C_v = \frac{3}{2} n_e k$ and $\partial \ln n_e / \partial z = \zeta$. Inserting typical values in (56) (see Section 11) we find for $T_0 \approx 1$ keV and $\alpha \approx 1/\Delta r$ that ω varies from 5×10^9 to 5×10^{12} sec^{-1} depending on n_e. Such a frequency represents a short time scale compared with a laser pulse length of 5×10^{-9} sec.

In the numerical solution of (53)–(55) the $E_z J_z$ term may be represented as either (see Fig. 2)

$$(E_z J_z)_{0,0} = -\frac{1}{2}\left(\frac{kT}{e}\,\zeta J_z\right)_{+,0} - \frac{1}{2}\left(\frac{kT}{e}\,\zeta J_z\right)_{-,0} \tag{57a}$$

or

$$(E_z J_z)_{0,0} = -\left(\frac{kT}{e}\,\zeta\right)_{0,0} \frac{1}{2}(J_{z+,0} + J_{z-,0}). \tag{57b}$$

If Eq. (53) is solved explicitly as regards T_e, then the amplification factor of a mode $T_1 \sim \exp(ikj\Delta)$ is

$$A = 1 - 2s(1 + \cos k\Delta) \qquad \text{or} \qquad A = 1 - 4s \tag{58a), (58b)}$$

using (57a) and (57b), respectively; the quantity

$$s = \frac{2}{3n_e}\frac{k}{e}\,\zeta J_z\,\Delta t$$

is assumed constant in r. Therefore if a disturbance is excited during a calculation the time-step control

$$\Delta t^{n+3/2} \leqslant \delta \left| \frac{Q^n}{Q^{n+1} - Q^n} \right|_{\max} \Delta t^{n+1/2}$$

will enforce values satisfying ($\omega_{\max}$ is the maximum value of (56))

$$\omega_{\text{num}} = \frac{2\pi}{\Delta t} \approx \omega_{\max}.$$

This was found to cause problems as mentioned earlier.

If Eq. (53) is solved implicitly as regards T_e (ADI method, see Appendix A3), then the amplification factors of a mode during the r-sweep and z-sweep are for (57a) and (57b), respectively

$$A_r = \frac{1}{1 + s(1 + \cos k\Delta)}, \qquad A_z = \frac{1 - s\cos k\Delta}{1 + s}, \tag{59a}$$

$$A_r = A_z = \frac{1}{1 + 2s}. \tag{59b}$$

The amplification factors (58) and (59) have here zero imaginary parts; in general A is complex because s is not constant so that modes propagate. While (59b) damps all modes it is interesting to note that (59a) only damps modes with $k\Delta \neq \pi$ (wavelength of two cells). The more natural choice (57a) of defining E_z and J_z at the same point

$(+, 0)$ using $T_{+,0} = \frac{1}{2}(T_{++,0} + T_{0,0})$ does not eliminate the shortest wavelengths which the calculation mesh can accommodate. In general these short wavelength modes may grow because of the nonlinear coupling between T and B (e.g., (53)–(55)). Although such modes are not at all well represented in a calculation anyway [24, 30] and should be eliminated as they represent "numerical waves" because of the restriction $k \leqslant k_{\max}$, they can give rise to problems. The choice (57b) implies a damping of these modes and a further damping occurs in part 2 of the diffusion stage. If this damping is insufficient additional artificial smoothing can be introduced.

9. Choice of Transport Coefficients

All the transport coefficients begin with the classical expressions as given in [14, 18, 20]. Additional physical processes can be included via anomalous transport coefficients. Several papers on lasser-produced plasmas have discussed this issue. For all fluxes F we impose upper limits $F_{\max}$ via the flux limit model used in [4]

$$\frac{1}{F} = \frac{1}{F_{\text{class}}} + \frac{1}{F_{\max}},$$

where F_{class} is the classical flux usually of the form $\alpha \nabla Q$; this expression modifies the coefficient α. The maximum fluxes allowed are the free streaming fluxes $\sim \frac{1}{4} nukT$ for ion and electron thermal transport and the blackbody flux $\sim \sigma T_e^4$ for radiation transport. The maximum transverse electron flux is $\sim n_e u_e \rho_e \nabla T_e$ and similarly for the ion transverse flux. In the low-density corona region the current densities $J \sim e n_e U_J$ can give rise to high drift velocities (runaway situations) and an anomalous resistivity can be included to maintain $u_J \ll u_e$.

10. Boundary Conditions

Because our model is essentially Eulerian the boundaries of the calculation mesh do not correspond to real physical boundaries. The choice of boundary conditions is therefore to some extent ambiguous. During the development of our model various conditions have been tried out especially those concerning the magnetic field. At the inner r-boundary, $r = 0$ cylinder symmetry is used.

At the outer r-boundary and the z-boundaries, free flow conditions $\nabla p = 0$ are used together with $\nabla n = 0$ and $\nabla T = 0$. The thermal fluxes are all zero at the boundaries and part of the radiative flux (Eq. (16)) is determined via $T_R = T_{\text{room}}$ at the boundaries.

The total electric field parallel to the boundary can be set to zero so that we can regard the plasma blowing off the target as surrounded by a flux-conserving sieve which lets through plasma but no magnetic flux. Alternatively the current density **J** normal to the boundary can be set to zero and this condition has been used in the calculations described in the next section.

11. Results

All calculations discussed here are carried out for a fixed target and laser performance. The target material is carbon and the size is $R_0 = 250\,\mu$m and $z_2 - z_1 = 800\,\mu$m. The mesh used is $(N_r, N_z) = (10, 40)$ with initial temperatures of 1 eV. The density profile varies initially only with z and increases exponentially from $10^{-6}n_s$ to n_s over $700\,\mu$m (n_s is solid density). The laser-illumination profile is assumed Gaussian in r and t with half widths $100\,\mu$m and 2.2 nsec, respectively; the wavelength is $\lambda = 1.06\,\mu$m (Nd) and the energy available in the pulse is 18 J.

We consider the following six calculations labeled 1–6, all of which employ classical transport coefficients including the flux limits of Section 9:

1. Three temperature calculation with no hydrodynamics and no magnetic fields. Diffusion by the splitting method.
2. As 1 but diffusion by the ICCG method.
3. As 2 but no radiation temperature.
4. Two-temperature calculation (T_e, T_i) with hydrodynamics and magnetic fields. Diffusion by the ICCG method. $\mathbf{E} \cdot \mathbf{J}$ treated explicitly where $\mathbf{E}$ contains only the electron pressure. $D_\wedge = G_\wedge = G_\perp = 0$.
5. As 4 but $\mathbf{E} \cdot \mathbf{J}$ treated implicitly.
6. As 5 with $D_\wedge$, $G_\wedge$, and $G_\perp$ treated implicitly.

Calculations 1–3 look at the differences between the splitting and the ICCG methods as well as the effects of radiation transport although these are relatively small for the present laser-target setup. Calculations 4–6 study the response from the code when magnetic fields are included.

Two-dimensional codes produce a massive amount of information which could easily swell this paper. The following figures show curves which have been chosen to bring out the main differences between the results of cases 1–6. Typical temperature profiles, see for example [6, 7, 15], are shown for case 2 in Fig. 3; the profiles are taken along the axis $r = 0$ at two different times. Similar profiles with lower values of T are found for $r > 0$. For all calculations we evaluate the time–space integrated emission spectrum

$$S(\nu) = \int_0^{t_0} \Psi(\nu)\, dt,$$

where $\Psi(\nu)$ is given by (15) and (16). $S(\nu)$ is a sensitive indicator of the entire time history of the temperatures. The spectrum $S(\nu)$ has the shape given in Fig. 4 (case 2) and the slope corresponds to an "effective" temperature of 600–700 eV. Figure 5 shows the ratios

$$r_{12} = S_1(\nu)/S_2(\nu), \qquad r_{23} = S_2(\nu)/S_3(\nu),$$

the subscripts referring to the calculation number. There is agreement to within 10 % between S_1 and S_2 in the interval 0.9 to 4 keV. At low energies (~400 eV) the splitting

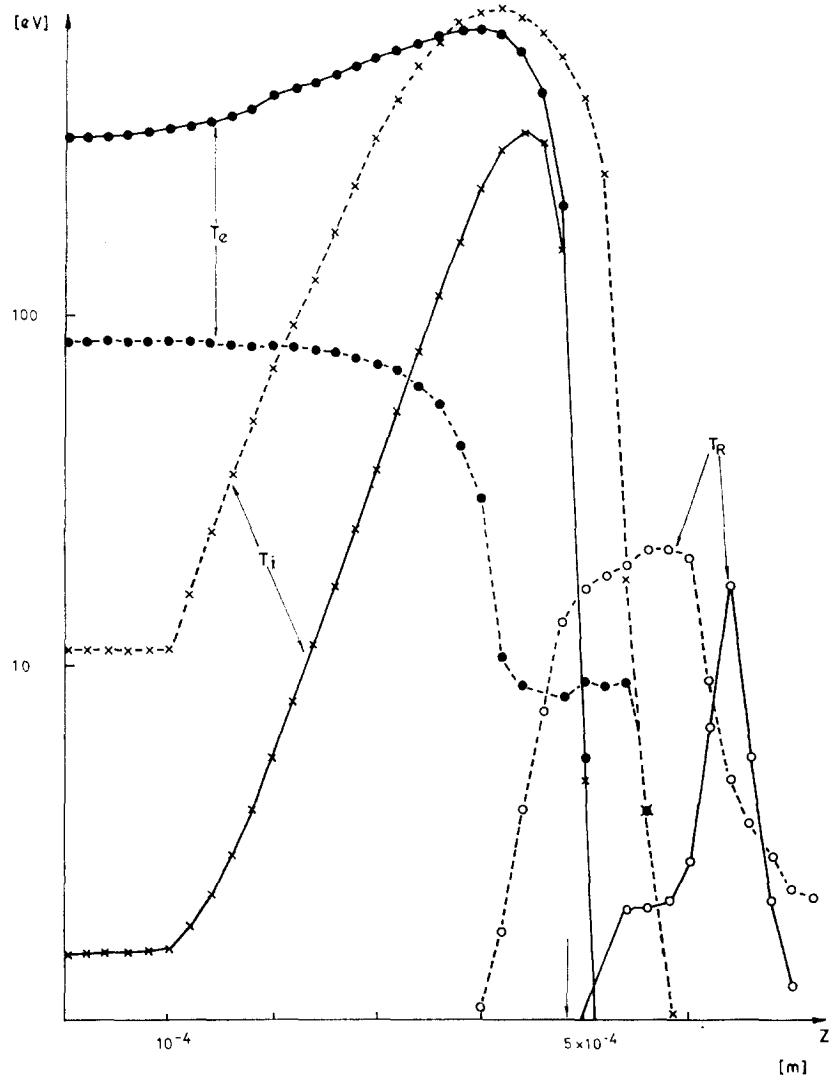

FIG. 3. Axial temperature profiles for case 2 (ICCG diffusion). Full curves are at $t = 0 \cdot 4$ nsec; dashed curves, at $t = 8 \cdot 0$ nsec. The same profiles for case 1 look similar except the one for T_R. The arrow at $z = 480$ μm indicates position of critical density.

method predicts about 25% more radiation than the ICCG method because the former method propagates the electron energy deeper into the solid regions. The discrepancy at the high-energy tail originates from the predicted temperatures at those few mesh points occupying a small axial region near the critical density. The curve representing r_{23} shows the change in $S(\nu)$ due to radiation transport. The enhancement at low energies (< 300–400 eV) is caused by propagation of the radiation field

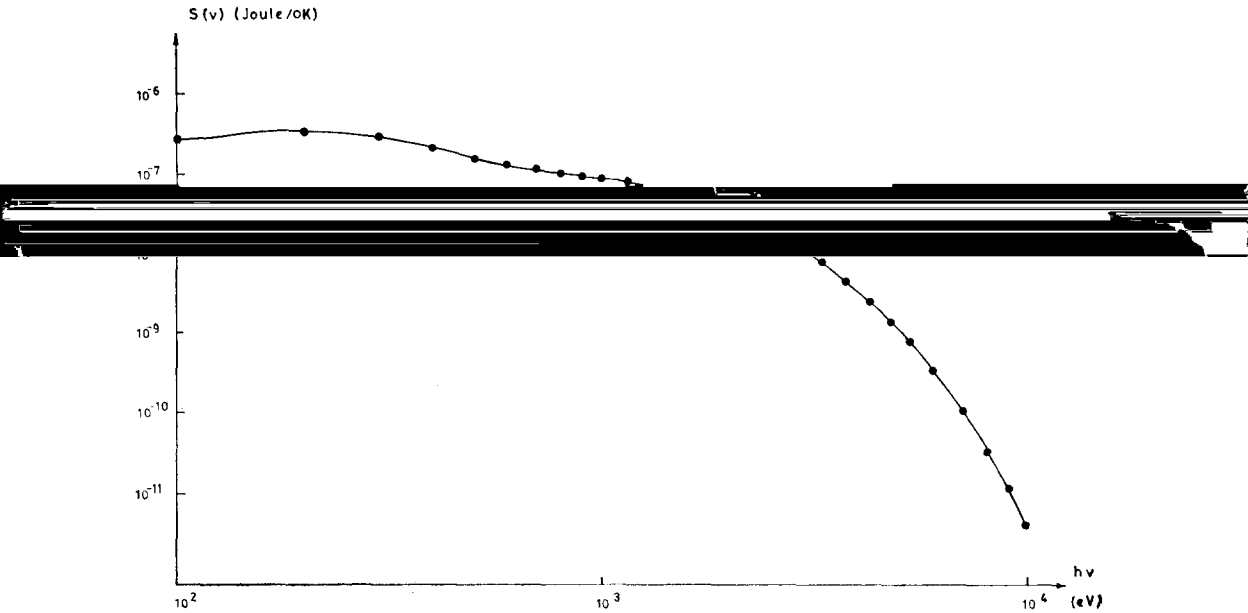

FIG. 4. Radiation emission spectrum for case 2.

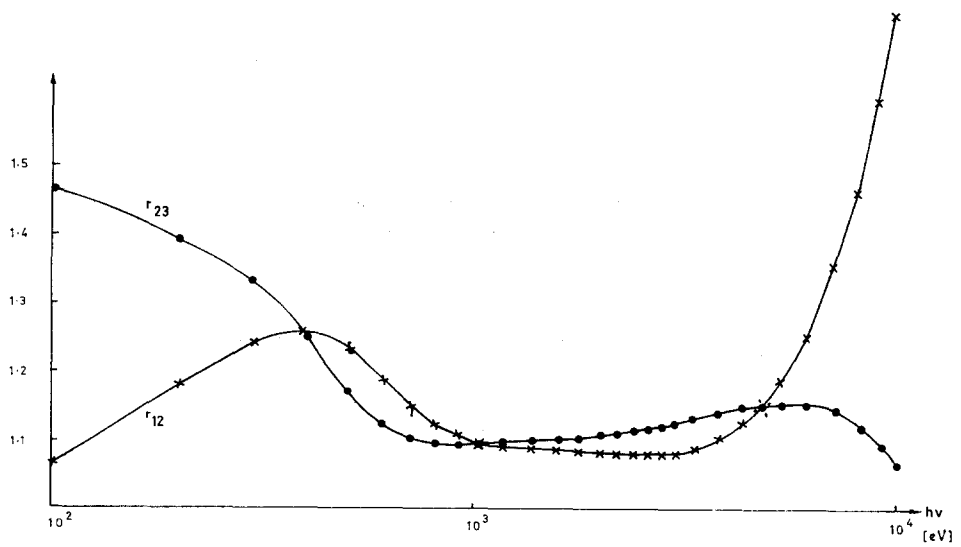

FIG. 5. Ratios between emission spectra obtained in cases 1, 2, and 3. (Diffusion by splitting, ICCG, and ICCG but no radiation temperature, respectively.)

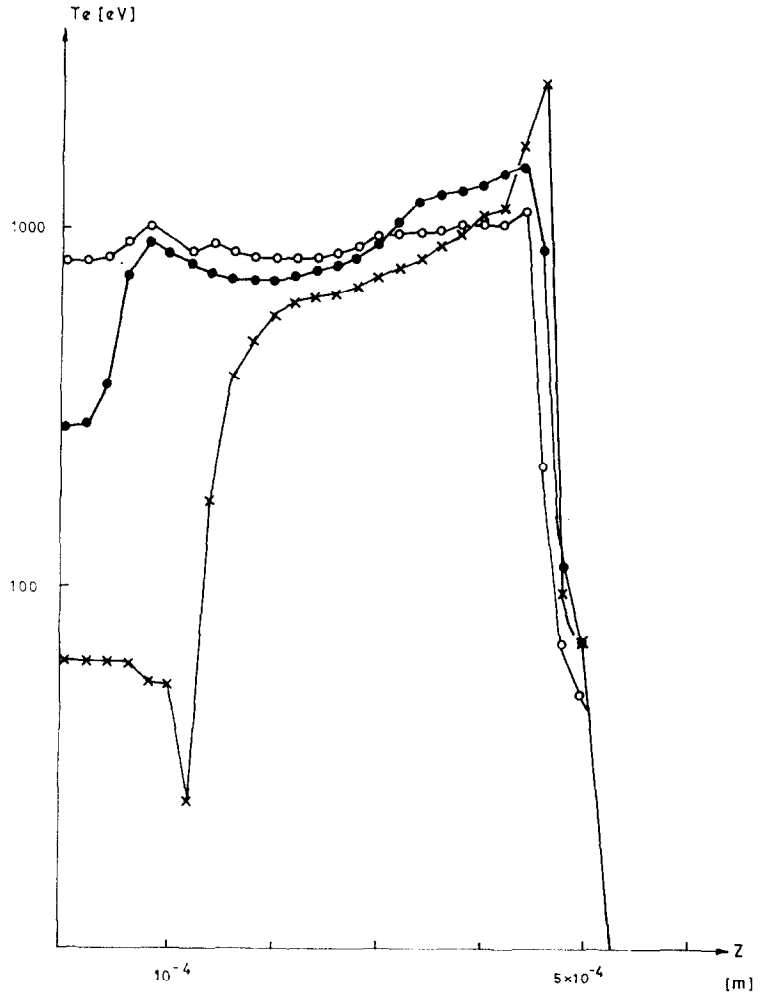

FIG. 6. Axial electron temperature profiles for case 4 (explicit $\mathbf{E} \cdot \mathbf{J}$) : ×, $t = 0.55$ nsec; case 5 (implicit $\mathbf{E} \cdot \mathbf{J}$) : ·, $t = 0.54$ nsec; case 6 (implicit $\mathbf{E} \cdot \mathbf{J}$ and transport) : ∘, $t = 0{,}56$ nsec.

into the solid regions followed at later times by a (relatively) small energy transfer to the cold electrons.

The results from calculations 4–6 are shown in Figs. 6 and 7. The time chosen is ~0.5 nsec because calculation 4 could not be carried on much further. Figure 6 depicting the axial T_e profile shows a substantial difference between cases 4 and 5, i.e., between explicit and implicit treatment of $\mathbf{E} \cdot \mathbf{J}$. The difference between the calculated $S_4(\nu)$ and $S_5(\nu)$ is however quite small (less than 10 %); the snapshot profiles of Fig. 6 differ because local oscillations of T_e are much larger for case 4 than for case 5. The same applies to the magnetic field profiles of Fig. 7 shown against z along $r = 100\ \mu$m.

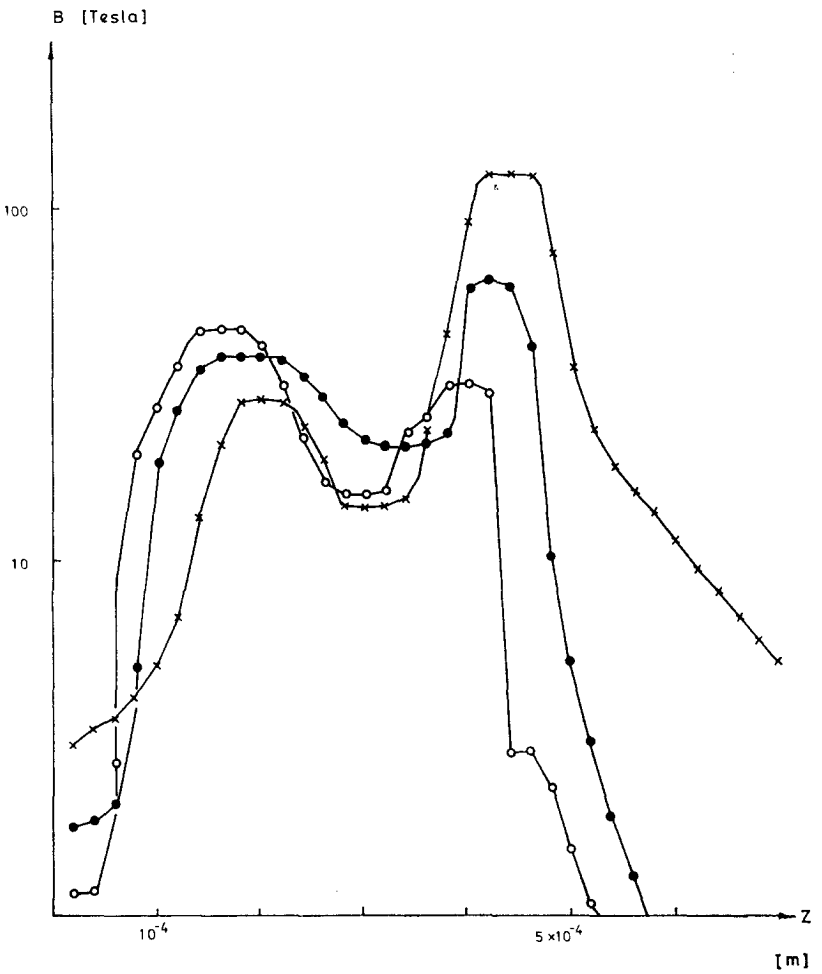

FIG. 7. Magnetic field against z at $r = 10^{-4}$ m. Legend as in Fig. 6.

The inclusion of thermoelectric effects, transverse fluxes, and the Hall term in calculation 6 shows a small change to T_e ; the magnetic field near the critical density is however smaller now since **E** is smaller (see (A2)).

It is our experience that results from calculations which include magnetic field effects should be treated with some care. Snapshot profiles such as those of Figs. 6 and 7 only become meaningful after some averaging over several time steps has been made. To emphasize this point we show in Fig. 8 for case 5, the temporal variation $\Delta \ln T_e$ of the axial temperature profile shown in Fig. 6 (full curve); the dashed curve displays $\Delta \ln T_e$ at a later time. For both curves we define

$$\Delta \ln T_e = | T_e^{n+1} - T_e^n | / T_e^n.$$

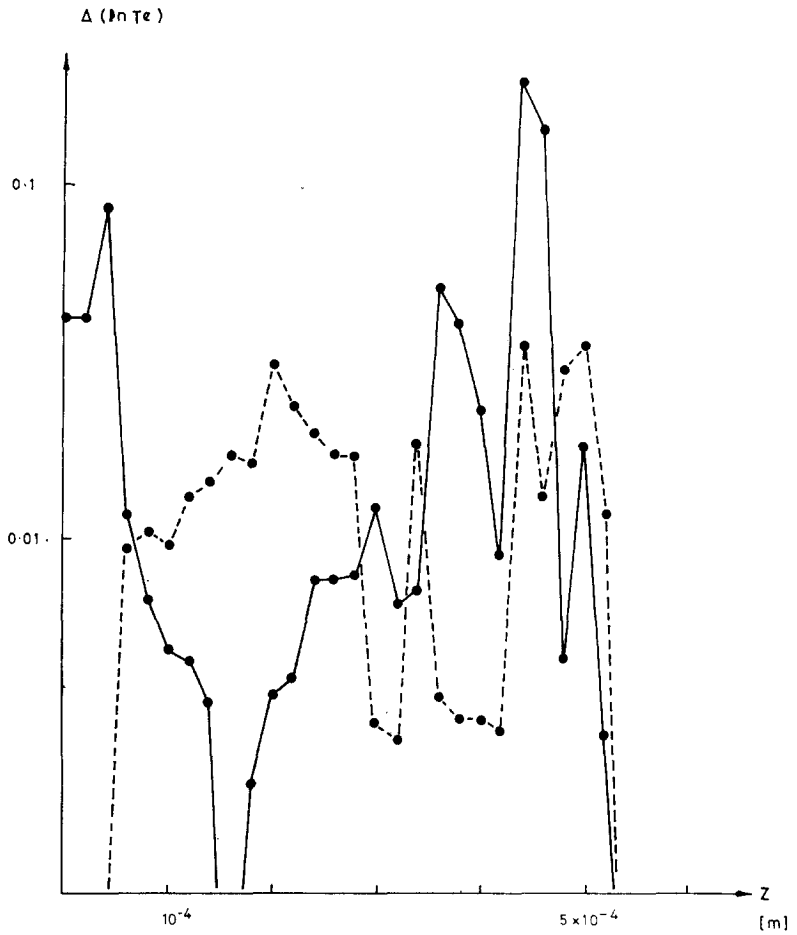

FIG. 8. Instantaneous change of axial electron temperature profiles for case 5. Full curve $t = 0 \cdot 55$ nsec. Dashed curve $t = 1 \cdot 0$ nsec.

The quantities $\Delta \ln Q$, where Q denotes the main variables, control the variation of the step length Δt whose variation with time is shown for case 5 at every 25 steps in Fig. 9; the restriction $\Delta \ln Q < 0.25$ has applied to all the calculations. The dashed curve in Fig. 9 represents the variation of Δt for case 5 when a smoothing algorithm (Appendix 6) is applied to T_e and B after part 1 of the diffusion stage.

Several conclusions can be drawn from these studies. When radiation is important, an implicit method (e.g., ICCG) should be used to maintain accuracy and to avoid lengthy calculations. When magnetic fields become large enough ($\omega_{ce}\tau > 1$), a very carefully chosen implicit algorithm (Eq. (50)) must be used for the $\mathbf{E}_s \cdot \mathbf{J}$. term. Even then the magnetic effects may display rapid time variations in other physical quantities, such as the electron temperature, and the results must be carefully interpreted.

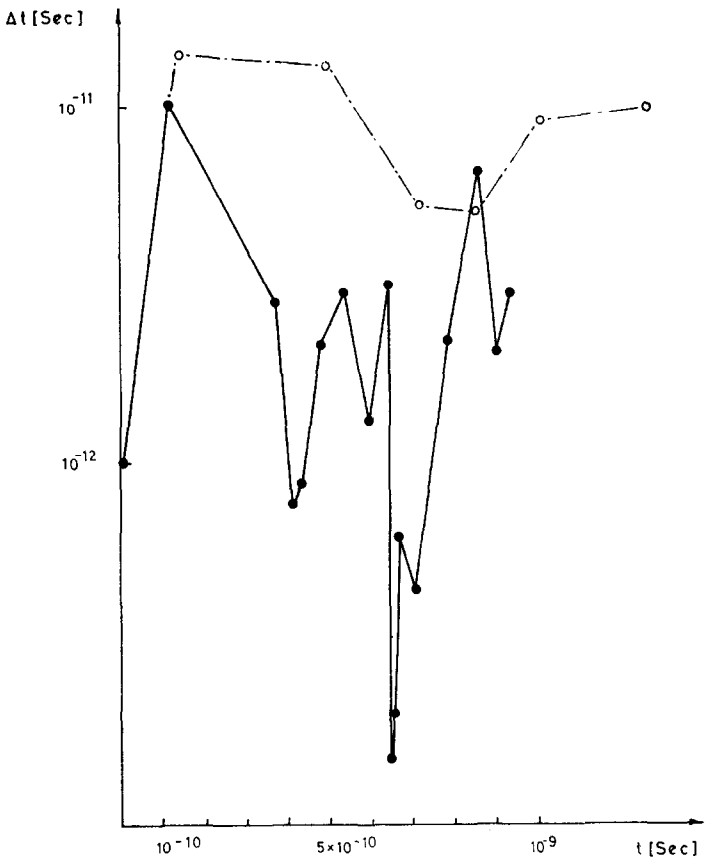

FIG. 9. Time variation of step length Δt for case 5. The separation between successive dots is 25 steps. The dashed curve shows the increase in Δt caused by a smoothing algorithm.

ACKNOWLEDGMENTS

The authors acknowledge useful discussions with G. J. Pert, K. V. Roberts, J. Magill, M. G. Haines, and G. Doherty who supplied the ICCG package.

APPENDIX

Here we shall briefly explain some of the details behind the numerical treatment of each of the terms of Eq. (38). The subscript indexes used are those explained in Fig. 2. Superscripts are dropped since it should be clear from Section 7 which value of $\mu = n + l/m$ is being used.

A.1. *The Diffusion Terms*

Five-point differencing is used for the term D and is regarded as sufficiently accurate because of the orthogonality of the mesh. The splitting method leads to two sets of equations

$$-a_r Q_{++,0} + b_r Q_{0,0} - c_r Q_{--,0} = d_r ,$$
$$-a_z Q_{0,++} + b_z Q_{0,0} - c_z Q_{0,--} = d_z ,$$

where, for example, for $Q = T_e$ and $\Delta v = r\Delta r\Delta z$

$$b_r \equiv C\Delta v + a_r + c_r = C\Delta v + \Delta t \left(r_+ \kappa_{+,0} \frac{\Delta z}{\Delta r_+} + r_- \kappa_{-,0} \frac{\Delta z}{\Delta r_-} \right),$$

$$b_z \equiv C\Delta v + a_z + c_z = C\Delta v + \Delta t \left(r\kappa_{0,+} \frac{\Delta r}{\Delta z_+} + r\kappa_{0,-} \frac{\Delta r}{\Delta z_-} \right),$$

$$d_r = d_z = C\Delta v T_{0,0} + \tfrac{1}{2}\Delta t(S + A).$$

For brevity subscripts $\perp$ and e have been dropped. Similar expressions apply to the coefficients a, b, c, and d of the other equations. The ICCG method results in the matrix equation (44) with $\underline{\mathbf{a}}$ being a symmetric $M \times M$ matrix. The elements of $\underline{\mathbf{a}}$ denoted by e (to avoid confusion) are on the diagonal (k, k corresponds to point 0, 0)

$$e_{kk} = b_r + b_z - C\Delta v.$$

The off-diagonal elements are

$$e_{k+1,k} = -a_r , \; e_{k-1,k} = -c_r ,$$
$$e_{k,k+1} = -a_z , \; e_{k,k-1} = -c_z ,$$

while

$$b_k = C\Delta v Q_{0,0} + \Delta t(S + A).$$

Although the splitting and ICCG method can be applied to the variables T_e, T_i, T_r, and B in any combination we have found (not unexpectedly) that the biggest difference in the results produced by these methods occurs for the T_e and T_R equations since D_i and D_b are more diagonally dominant than D_e and D_R.

A.2. *Transverse Fluxes and Fields*

The $D_\wedge$ terms describing heat flow along the isotherms (or the Hall field) are differenced in the same way as in [23], e.g.,

$$\begin{aligned} 4\Delta v D_\wedge = {} & r_+ \kappa_{+,0}(T_{++,++} - T_{++,--} + T_{0,++} - T_{0,--}) \\ & - r_- \kappa_{-,0}(T_{0,++} - T_{0,--} + T_{--,++} - T_{--,--}) \\ & - r\kappa_{0,+}(T_{++,++} + T_{++,0} - T_{--,++} - T_{--,0}) \\ & + r\kappa_{0,-}(T_{++,0} + T_{++,--} - T_{--,0} - T_{--,--}). \end{aligned}$$

A.3. *Thermoelectric Fields and Fluxes*

The symmetry of the kinetic coefficients $\beta_\perp$ and $\beta_\wedge$ (the Onsager principle) implies that

$$\mathbf{E}^\beta \cdot \mathbf{J} - \nabla \cdot \mathbf{q}^\beta = \frac{k}{e} T_e \nabla \cdot (\underline{\beta} \cdot \mathbf{J}), \tag{A3}$$

where $E^\beta = -(k/e)\,\underline{\beta} \cdot \nabla T_e$ and $q^\beta = -(k/e)\,T_e \underline{\beta} \cdot \mathbf{J}$ are the thermoelectric field and flux whose curl and divergence are represented by the G terms. It is desirable to retain the identity (A3) when the G terms are differenced. This is however not possible for the components of (A3) involving $\beta_\perp$ as long as B and T_e are expressed at the same mesh −points. The problem is that E_r^β is required at points $(0, +)$ and $(0, -)$, while q_r^β is required at points $(+, 0)$ and $(-, 0)$, and vice versa for the z-components. A remedy for the discrepancy between the identity (A3) and the corresponding finite-difference expression is to solve that part of (50b) which includes $\beta_\perp$ terms on a staggered mesh on which B is expressed at the points $(-, -)$, $(+, -)$, $(-, +)$, etc. (see Fig. 2). However it is not possible to reapportion both magnetic flux and energy from the staggered mesh points to the ordinary mesh points in a conservative fashion.

The differencing of the $G_\perp$ terms (39d) and (42d) follows [23, 29], while the differencing of the $G_\wedge$ terms (39e) and (42e) is the same as for D. In these terms the electron temperature is always treated implicitly and the same applies to S_b. The electric field is

$$E_{z+,0} = \tfrac{1}{2}(E_{z0,0} + E_{z++,0}),$$
$$E_{z0,0} = -(k/e)(\zeta_{0,0} T_{0,0} + \beta_{\perp 0,0}\,(T_{0,++} - T_{0,--}) - \beta_{\wedge 0,0}(T_{++,0} - T_{--,0})),$$

and similarly for E_r. The energy transfer rate $E_z J_z \Delta v$ as B changes from B^0 to B^* is

$$(E_z \bar{J}_z)_{+,0}\,(r\Delta r)_+\,\Delta z_0\,.$$

This rate is split such that

$$\tfrac{1}{2} E_{z0,0} \bar{J}_{z+,0} (r\Delta r)_+\,\Delta z_0$$

is taken from cell $(0, 0)$ and

$$\tfrac{1}{2} E_{z++,0} \bar{J}_{z+,0} (r\Delta r)_+\,\Delta z_0$$

is taken from cell $(++, 0)$ and similarly for $E_r J_r \Delta v$. The average $\bar{J}_z$ is $\bar{J}_z = \tfrac{1}{2}(J_z^0 + J_z^*)$ [26].

A.4. *Energy Exchange Terms*

The exchange of energy between ions and electrons A_i (Eq. (40g)) and the exchange of energy between electrons and the radiation field A_R (Eq. (41g)) can occur at very rapid rates, i.e., $\omega_{ei}\,\Delta t$ or $\omega_{eR}\,\Delta t$ can vary over many orders of magnitude. The

numerical treatment is an extension to the method described in [32] and also used in [4]. From Eqs. (38) we form

$$\frac{\partial \xi}{\partial t} = \phi_{ei} - \lambda_{11}\xi - \lambda_{12}\chi,$$
$$\frac{\partial \xi}{\partial t} = \phi_{er} - \lambda_{21}\xi - \lambda_{22}\chi, \tag{A4}$$

where

$$\xi = T_e - T_i, \qquad \chi = T_e - T_R, \qquad \phi_{ei} = \frac{w_e}{C_{ve}} - \frac{w_i}{C_{vi}}, \qquad \phi_{er} = \frac{w_e}{C_{ve}} - \frac{w_R}{C_{vR}},$$

and

$$w = D + D_\wedge + G_\perp + G_\wedge + S;$$

the λ's involve ω_{ei}, ω_{eR}, and the reciprocal specific heats. Equation (A4) is solved by the exponential relaxation method of [32] and yields the expressions

$$\langle \xi \rangle = A_{11}\langle e^{-\omega_1 t} \rangle + A_{12}\langle e^{-\omega_2 t} \rangle + B_1$$

and similarly for $\langle \chi \rangle$, A_{11}, A_{12}, and B_1 depend on the ϕ's and the initial values ξ_0, and χ_0; the bracketed terms are the correctly averaged values as explained in [32] and ω_1 and ω_2 are the roots of a quadratic equation with the λ's as coefficients. The exchange terms (40g) and (41g) using the calculated values of $\langle \xi \rangle$ and $\langle \chi \rangle$ then enter the diffusion equations (52) as source terms.

A.5. *The Remaining Source Terms*

The calculation of S_e involves three terms (Eq. (39f)) of which P_{bb} is straightforward. The laser deposition term is calculated by

$$-\frac{\partial}{\partial z} F_L = -\frac{1}{\Delta z}(F_{0,+} - F_{0,-}) = \frac{1}{\Delta z} F_{0,-}(1 - e^{-I}),$$

where $I = \int_{z-}^{z+} \alpha dz$ and α given by Eq. (31). Because of the dependence of α upon $\xi = n_e/n_c$ it is necessary to consider weak and strong spatial variations in n_e separately. For weak variations in n_e (or ξ) we have

$$\int_{z-}^{z+} \xi^2(1 - \xi)^{-1/2}\, dz = \xi_0^2(1 - \xi_0)^{-1/2}\, \Delta z.$$

For strong variations of ξ we fit two exponential curves to the density profile between points (z_{--}, z_0) and (z_0, z_{++}) respectively in order to estimate ξ at the points z_- and z_+. The integration is carried out yielding

$$\int_{z-}^{z+} \xi^2(1 - \xi)^{-1/2}\, dz$$
$$= \frac{2}{3}\frac{1}{(\ln \xi_1 - \ln \xi_2)}((2 + \xi_1)(1 - \xi_1)^{1/2} - (2 + \xi_2)(1 - \xi_2)^{1/2})\, \Delta z$$

where $\xi_1 = (\xi_{--}\xi_0)^{1/2}$ and $\xi_2 = (\xi_0\xi_{++})^{1/2}$. The integrations can be carried up to $\xi_2 = 1$, i.e., the critical density whose coordinate z_c is found from the exponential fits. Further deposition of energy (see (32)) occurs over an interval of order Δz and contributes to those two cells whose coordinates are on either side of z_c. Reflection of light follows the same procedure.

A.6. *Smoothing*

To speed up a calculation a smoothing algorithm can be applied to eliminate short wave length disturbances. The algorithm used represents explicit diffusion of a quantity Q with a diffusion coefficient

$$D = C_1 \Delta r \Delta z / \Delta t \qquad \text{if } \Delta \ln Q > C_2,$$
$$D = 0 \qquad \text{if } \Delta \ln Q < C_2,$$

where the constants C_1 and C_2 are of order 0.1–0.2 and $\Delta \ln Q$ is the relative change in Q during part 1 of the diffusion stage.

REFERENCES

1. J. NUCKOLLS, L. WOOD, A. THIESSEN, AND G. ZIMMERMAN, *Nature (London)* **239** (1972), 139.
2. J. STAMPER AND D. TIDMAN, *Phys. Fluids* **16** (1973), 2024.
3. E. B. GOLDMAN, *Plasma Phys.* **15** (1973), 289.
4. J. P. CHRISTIANSEN, D. E. T. F. ASHBY, AND K. V. ROBERTS, *Comput. Phys. Comm.* **7** (1974), 271.
5. G. S. FRALEY, A. J. LINNEBUR, R. J. MASON, AND R. L. MORSE, *Phys. Fluids* **17** (1974), 474.
6. D. G. COLOMBANT, K. G. WHITNEY, D. A. TIDMAN, N. K. WINSOR, AND J. DAVIS, *Phys. Fluids* **18** (1975), 1687.
7. R. S. CRAXTON AND M. G. HAINES, *Phys. Rev. Lett.* **35** (1975), 1336.
8. H. D. SHAY *et al.*, Livermore Report UCRL — 75465, 1974; G. ZIMMERMAN, Livermore Report UCRL — 74811, 1973.
9. A. A. AMSDEN AND C. W. HIRT, Los Alamos Report LA-5100, 1972.
10. J. P. CHRISTIANSEN AND N. K. WINSOR, *Comput. Phys. Comm.* **17** (1979), 397.
11. R. S. CRAXTON AND R. L. MCCRORY, Rochester Lab. for Laser Energetics, Annual Report, 1977.
12. D. MOSHER, NRL Report 2563, 1973.
13. J. MAGILL, *J. Phys. D: Appl. Phys.* **10** (1977), 2257.
14. S. I. BRAGINSKII, "Reviews of Plasma Physics," (M. A. Leontovich, Ed.), Consultants Bureau, New York, 1965).
15. N. K. WINSOR AND D. A. TIDMAN, *Phys. Rev. Lett.* **31** (1973), 1044.
16. J. P. BORIS AND D. L. BOOK, *J. Computational Phys.* **11** (1973), 38; D. L. BOOK, J. P. BORIS, AND K. HAIN, *J. Computational Phys.* **18** (1975), 248.
17. R. S. CRAXTON AND R. L. MCCRORY, *J. Computational Phys.* **33** (1979), 432.
18. D. H. SAMPSON, "Radiative Contributions to Energy and Momentum Transport in a Gas," Interscience, New York, 1965.
19. D. D. CLAYTON, "Principles of Stellar Evolution and Nucleosynthesis," McGraw-Hill, New York, 1968.
20. L. SPITZER, "Physics of Fully Ionized Gases," Interscience, New York, 1965.
21. J. B. CHASE, J. L. LEBLANC, AND J. R. WILSON, *Phys. Fluids* **16** (1973), 1142.

22. T. W. JOHNSTON AND J. M. DAWSON, *Phys. Fluids* **16** (1973), 722.
23. K. D. MARX AND J. KILLEEN, "Methods of Computational Physics," Vol. 9, Academic Press, New York, 1970.
24. D. E. POTTER AND K. V. ROBERTS, "Methods in Computational Physics," Vol. 9, Academic Press, New York, 1970.
25. M. L. WATKINS, M. H. HUGHES, K. V. ROBERTS, P. M. KEEPING, AND J. KILLEEN, "Methods in Computational Physics," Vol. 16, Academic Press, New York, 1976, J. HOGAN, *ibid.*
26. J. P. CHRISTIANSEN AND K. V. ROBERTS, *J. Computational Phys.* **28** (1978), 279.
27. G. J. PERT, R. S. CRAXTON, AND K. V. ROBERTS, private communication.
28. G. J. PERT, *J. Plasma Phys.* **18** (1977), 227.
29. I. R. LINDEMUTH AND J. KILLEEN, *J. Computational Phys.* **13** (1973), 181.
30. R. D. RICHTMEYER AND K. W. MORTON, "Difference Methods for Initial Value Problems," Interscience, New York, 1967.
31. D. S. KERSHAW, *J. Computational Phys.* **26** (1978), 43.
32. J. P. CHRISTIANSEN AND K. V. ROBERTS, *J. Computational Phys.* **17** (1975), 332.